AIP Review of Scientific Instruments

Smith-chart diagnostics for multi-GHz time-domain-reflectometry dielectric spectroscopy

N. E. Hager, R. C. Domszy, and M. R. Tofighi

Citation: Rev. Sci. Instrum. **83**, 025108 (2012); doi: 10.1063/1.3685248
View online: http://dx.doi.org/10.1063/1.3685248
View Table of Contents: http://rsi.aip.org/resource/1/RSINAK/v83/i2
Published by the American Institute of Physics.

Smith-chart diagnostics for multi-GHz time-domain-reflectometry dielectric spectroscopy

N. E. Hager III,[1,2,a)] R. C. Domszy,[1,2] and M. R. Tofighi[3]
[1]*Department of Physics and Engineering, Elizabethtown College, Elizabethtown, Pennsylvania 17022, USA*
[2]*Material Sensing & Instrumentation, Inc., 772 Dorsea Rd., Lancaster, Pennsylvania 17601, USA*
[3]*Electrical Engineering, The Pennsylvania State University at Harrisburg, Middletown, Pennsylvania 17057, USA*

(Received 14 December 2011; accepted 28 January 2012; published online 13 February 2012)

A time-domain-reflectometry Smith-chart display is demonstrated to be a valuable diagnostic tool in a variety of situations in time-domain-reflectometry dielectric spectroscopy. A relative reflection coefficient is formed by dividing the Laplace transform of the reflected sample transient by the Laplace transform of the empty-sensor transient and displaying in the complex plane, with the approximate sensor admittance read from susceptance and conductance circles. The Smith chart provides, as a diagnostic tool, an initial estimate of the dielectric behavior in the multi-GHz range and a means of identifying artifacts in acquisition and Laplace transform, in a way which does not require multiple steps of calibration and is only one step removed from the direct transient. Results are presented for a simple 3.5-mm flat sensor immersed in various liquid media, showing variations in the Smith chart for typical variations in sample permittivity, loss, and conductivity. Results are matched to vector network analyzer (VNA) measurement over an identical frequency range, as well as to finite-element field simulation. Results are also presented for a 3.5-mm sensor with various terminating pin lengths, typically employed at low frequencies and low permittivity media to increase sensor capacitance. For an unshielded pin, the Smith chart detects reflections from sample boundaries and measures the effectiveness of shielding used to eliminate these reflections. For a shielded pin, it characterizes the effect of pin length on the susceptance variation and the onset of pin resonance at high frequencies and high-permittivity values. The effect of artifacts appearing in the Smith chart on the actual calibration is shown by tracking them through the calibration process to the final result. Results are also presented for a 9-mm flat termination used for concrete hydration monitoring, showing effects of transmission-line discontinuities within a terminating plug and the onset of waveguide-like modes in a surrounding shield, with results compared to VNA measurement. *© 2012 American Institute of Physics*. [http://dx.doi.org/10.1063/1.3685248]

I. INTRODUCTION

Time-domain-reflectometry (TDR) dielectric spectroscopy[1] is a popular method for obtaining complex permittivity of materials at microwave frequencies. The sample is interrogated with a rapid voltage pulse, with the returning reflection captured and converted to complex permittivity by Laplace transform. Signals originating from the sample are separated from artifacts originating in the instrument and connecting lines according to propagation delay, providing an intuitive time-of-flight interface for materials researchers not familiar with microwave techniques. Equipment costs are relatively low compared with conventional vector network analyzers (VNA).

A main limitation is the difficulty in obtaining reliable information at multi-GHz frequencies, particularly using inexpensive single-use sensors. Small instrumental artifacts can be captured in the reflected signal along with dielectric response, which though not evident in the full-scale transient, become accentuated by the Laplace transform and differential methods used in processing and calibration. Such artifacts may originate from radiation from the sensor, reflections from sample boundaries, resonance of the sensing pin, reflections from support spacers near the measurement plane, and coupling to waveguide modes in any shielding arrangement. Sensor radiation, for example, can reflect from sample boundaries producing delayed artifacts; while a castle-nut shield,[2] placed over the sensor tip, blocks radiation in the lateral direction and eliminates these artifacts. The shield works well for small-diameter sensors but not for large-diameter sensors (~9 mm) intended to average volume inhomogeneities near the sensor in concrete hydration monitoring.[2] For such large diameter sensors the required shield diameters are larger than allowed to avoid waveguide modes, and the antenna resonance effect tends to shift to lower frequencies as the aperture size increases. These problems are exacerbated by the use of inexpensive disposable sensors in concrete hydration monitoring, where variations may exist between sensors, as well as the need to engineer sensors with different terminating capacitances for different water/cement ratios. All of these problems introduce small artifacts into the process which are not evident in the direct transient, but become so when Laplace transform and multiple steps of calibration are performed. The

a)Electronic mail: nehager@msi-sensing.com.

result is a disconnect between input data and calibrated result where errors are difficult to trace and correct.

In this paper we present a simple Smith-chart method of assessing sensor behavior in the multi-GHz range, which is obtained directly from the reflected transient and can diagnose a variety of artifacts quickly before time-consuming calibration is performed. A relative reflection coefficient is obtained from the sample and empty-sensor reflections and displayed in the complex Smith-chart plane, with the approximate sensor admittance read from the additional susceptance and conductance circles. Large variations in sample permittivity, loss, and conductivity all present unique signatures in the Smith chart diagram, so deviations from expected behavior can be identified and corrected. To demonstrate the merit of the Smith-chart display we evaluate the effect of different pin lengths, sensor diameters, and terminating plug thicknesses, as well as the effectiveness of any surrounding shield. Laplace transform and display algorithms can be hard-coded, allowing the user to toggle between transient and Smith-chart display as different configurations are evaluated.

We begin with a simple 3.5-mm flat termination and survey responses of typical dielectric materials in the Smith chart diagram. Results are matched to VNA measurement for identical sensor and materials, as well as to finite-element field simulation. We then consider several 3.5-mm protruding pin configurations, typically used to extend measurement to lower frequencies and lower permittivity materials, and explore variations in pin length and shielding and match results to field simulation in each case. The propagation of artifacts revealed by the TDR Smith chart is traced through the bilinear calibration process, and their effect on the final calibrated permittivity is shown. Finally, we consider a large-diameter 9-mm sensor used in cement hydration monitoring, and explore effects of the terminating plug thickness and the onset to waveguide modes in the surrounding shield.

II. BACKGROUND

The expressions governing TDR dielectric spectroscopy are described in the literature.[1] An incident voltage pulse $v_i(t)$ propagating along a transmission line of characteristic admittance G_c encounters a terminating capacitive sensor of admittance Y producing a reflected pulse $v_r(t)$. The terminating admittance is the total current-to-voltage ratio $G_c(v_i - v_r)/(v_i + v_r)$, where v_i and v_r are the Laplace transforms of the incident and reflected pulses, respectively. The terminating admittance is related to sample permittivity ε by $Y = i\omega\varepsilon C_o$, so the permittivity is written as

$$\varepsilon(\omega) = \frac{G_c}{i\omega C_o}\frac{v_i - v_r}{v_i + v_r}, \tag{1}$$

where C_o is the geometric capacitance of the open terminated sensor. It should be noted that Eq. (1) neglects radiation, as well as any frequency dependence of the capacitance which could be significant at higher frequencies.[3]

To establish a common time reference, the incident voltage is substituted by the empty sensor reflection, by writing Eq. (1) for both empty sensor and sample reflections and manipulating to eliminate v_i. The result is a reflection function $\rho(\omega)$ (referred to by Cole *et al.*[1]) of similar form

$$\rho(\omega) = \frac{G_c}{i\omega C_o}\frac{v_{r,r} - v_{r,x}}{v_{r,r} + v_{r,x}}, \tag{2}$$

where $v_{r,r}$ and $v_{r,x}$ are the reflected pulse's Laplace transforms for the empty sensor and sample reflections, respectively. The permittivity is then obtained from a differential expression,

$$\varepsilon(\omega) = \frac{\rho + 1}{1 - (\omega C_o/G_c)^2\rho}, \tag{3}$$

where $\varepsilon(\omega)$ approaches $\rho(\omega) + 1$ in the low frequency limit, and the denominator represents the deviation from this relation as the frequency increases.

Cole *et al.*[1] notes that Eq. (3) is of similar form to the admittance transform between input/output terminals of an arbitrary 2-terminal device. The transform from reflection function to permittivity is thus combined with the admittance transform along the transmission line between the TDR input and terminating sensor. Equation (3) is written in a bilinear form, where numerator and denominator terms are relaxed to unknown device parameters to be determined by calibration, thus removing transmission line and connector effects. The equation thus becomes

$$\varepsilon(\omega) = \frac{(1 + A)\rho + C}{1 - B\rho}, \tag{4}$$

where complex parameters A, B, and C are determined using calibration with known reference standards. Parameters A and B are determined by writing each as their real and imaginary components ($A = A' + iA''$, $B = B' + iB''$, $\varepsilon = \varepsilon' - i\varepsilon''$, $\rho = \rho' - i\rho''$) multiplying out,[1] and separating real and imaginary components of resulting equations. The result is

$$\begin{aligned} A' + \varepsilon' B' + \varepsilon'' B'' &= \left(\frac{\varepsilon - C}{\rho}\right)' - 1, \\ A'' - \varepsilon'' B' + \varepsilon' B'' &= \left(\frac{\varepsilon - C}{\rho}\right)''. \end{aligned} \tag{5}$$

A and B are found by performing two liquid calibrations against common empty-sensor reference, generating four simultaneous equations involving measured reflection functions $\rho_{\mathrm{cal},1}(\omega)$ and $\rho_{\mathrm{cal},2}(\omega)$ and known target permittivities $\varepsilon_{\mathrm{cal},1}(\omega)$ and $\varepsilon_{\mathrm{cal},2}(\omega)$. Real constant C is adjusted such that parameters A and B go to zero in the limit of low frequencies.

Equation (2) can also be written in terms of a *complex reflection coefficient* by dividing numerator and denominator by $v_{r,r}$ to yield

$$\rho(\omega) = \frac{G_c}{i\omega C_o}\frac{1 - \Gamma_{rel}}{1 + \Gamma_{rel}}, \tag{6}$$

where Γ_{rel} is the relative reflection coefficient of the unknown signal relative to the empty sensor signal,

$$\Gamma_{rel} = \frac{v_{r,x}}{v_{r,r}} = \frac{v_{r,x}/v_i}{v_{r,r}/v_i} = \frac{\Gamma_x}{\Gamma_r}, \tag{7}$$

and Γ_x and Γ_r are the absolute reflection coefficients for the sample and empty sensor reflections, respectively. The relative reflection coefficient Γ_{rel} thus approximates the absolute reflection coefficient Γ_x, provided the empty-sensor capacitance is small and empty-sensor reflection $v_{r,r}$ approximates the incident pulse v_i as an ideal open circuit.

Real and imaginary components of the relative reflection coefficient can now be plotted on the lower capacitive half of the complex Smith chart as a function of frequency, with the approximate sensor admittance read from the susceptance and conductance circles. Since Γ_{rel} is referenced to the empty-sensor reflection losses in the transmission line do not appear, and losses appearing on the Smith chart are due to sample losses. An increasing real permittivity produces an increasing sensor susceptance, following a path around the lower perimeter of the Smith chart, while an increasing sample loss produces an increasing sensor conductance, following a path which spirals inward on the Smith chart. Artifacts in acquisition and Laplace transform appear as deviations from this expected behavior, and since the reflection function $\rho(\omega)$ is derivable from the relative reflection coefficient in Eq. (6), anomalies appearing in Γ_{rel} foreshadow anomalies appearing in the final bilinear calibration. The TDR Smith chart thus provides a quick method for assessing sensor response and material characteristics in the multi-GHz range, which requires no calibration and is only one computational step removed from the direct TDR transient.

III. PROCEDURES

Signals are acquired with an Agilent 54750 TDR oscilloscope with a 54754A differential plug-in, which has a 35-ps internal voltage step and a 20-GHz detection bandwidth. Reflected signals are captured non-uniformly on consecutive linear time segments,[4] starting at 10 ps/cm and increasing to 500 μs/cm in an automated sequence. At the beginning of the sequence the incident pulse is captured and used as a timing reference, with a feedback algorithm adjusting the timing of all later segments to provide drift control. Small jitter between segments is further minimized by scanning the entire sequence repetitively and averaging, thus minimizing jitter between the incident and initial reflected pulses during sequencing. The incident pulse is captured with 2000 points at 50 fs/point, with subsequent segments reduced in size and acquisition rate to 200 points per segment. Other settings are typically 12 time segments, with 32$\times$ signal averaging for each segment, and eight repetitions of the entire sequence for a total acquisition time of 3-4 min. Since the scope is ac-coupled, a vertical correction is applied to each segment to remove dc offsets from electrochemical effects and splice it smoothly with the preceding segment.

To reduce excessive computation and noise the linear segmented data is interpolated onto a logarithmic time scale prior to Laplace transform, using cubic-spline algorithms found in most math software. Each segment is first run through a median smoothing filter to minimize noise and provide additional signal averaging. Then the smoothed data is interpolated linearly up to the peak of the reflected transient, and logarithmically for all times thereafter. The linear interpolation is spaced at 5 ps per point, consistent with a 100 GHz Nyquist sampling frequency which is well above the 20-GHz bandwidth of the scope. The logarithmic interpolation starts at 5 ps per point and increases at a rate of around 50–60 points per decade.[5]

The Laplace integration is performed over the interpolated data with the integration interval adjusted to the logarithmic data spacing. To eliminate computational problems where the sinusoidal variation exceeds the data point spacing, a modified trapezoidal rule is used where the data is integrated with the sinusoidal variation over each 2-point interval analytically, and then summed over all 2-point intervals numerically. The integration is truncated at an integer number of analysis cycles with a patch term added to extrapolate to the last analysis cycle exactly. In conducting materials where the transient does not decay to the open-circuit baseline by the end of the last segment an additional patch term is added: the last segment is exponentially fit to the open-circuit baseline and the final integral contribution calculated analytically. Also, since the Laplace integration is done relative to the open-circuit baseline while Eq. (2) assumes the baseline preceding the reflection, a term $\Delta v/i\omega$ is added to the Laplace output where Δv is the offset between baselines. Further details of these procedures are found in Ref. 4.

VNA measurements are made with a HP model 8720C VNA over the frequency range of 50 MHz–20.05 GHz, at 401 equally spaced frequency points. The VNA is first calibrated using standard open, short, and matched load calibrations with the measurement reference plane set to the end of the VNA cable. Then the 3.5-mm coaxial sensor, $\sim$30 cm in length, is connected to the VNA cable. Artifacts associated with the imperfect connection between the two cables are removed by the well-known time gating method, applied to the VNA data during post-processing utilizing MATLAB.[6] A fifth-order Chebychev filter with 0.1 dB ripple and a time gate-width of 1.6 ns centered around the desired reflected component at 3.05 ns is used. The results for each liquid are then time-gated and divided by the time-gated response for the air-terminated sensor, in order to obtain the relative reflection coefficient. For the 9-mm line, which is about 4-5 times longer, the time-gate width and center are modified accordingly.

The field simulation is performed using ANSOFT high-frequency structure simulator (HFSS), verson 12.1.0, which solves Maxwell's equation using the finite element technique in the frequency domain.The liquid is modeled as a cylindrical volume, with diameter and height of 75 mm, which is enclosed by absorbing boundary condition. The sensor is immeresed in the volume at a depth of 40 mm. Simulation is run on a Dell Vostro 430 PC with an i7 2.8 GHz Quad Core CPU and 16 MByte of RAM, and takes about 160 min to complete for 110 frequency points from 0.1 MHz to 20 GHz.

IV. RESULTS

A. 3.5-mm sensor: Flat termination

Initial measurements are made using a simple open coaxial termination into representative dielectric liquids of varying permittivity, loss, and conductivity. Measurements are made with a 30 cm length of 3.5-mm semirigid coaxial line (MicroCoax UT-141) with one end ground mechanically flat

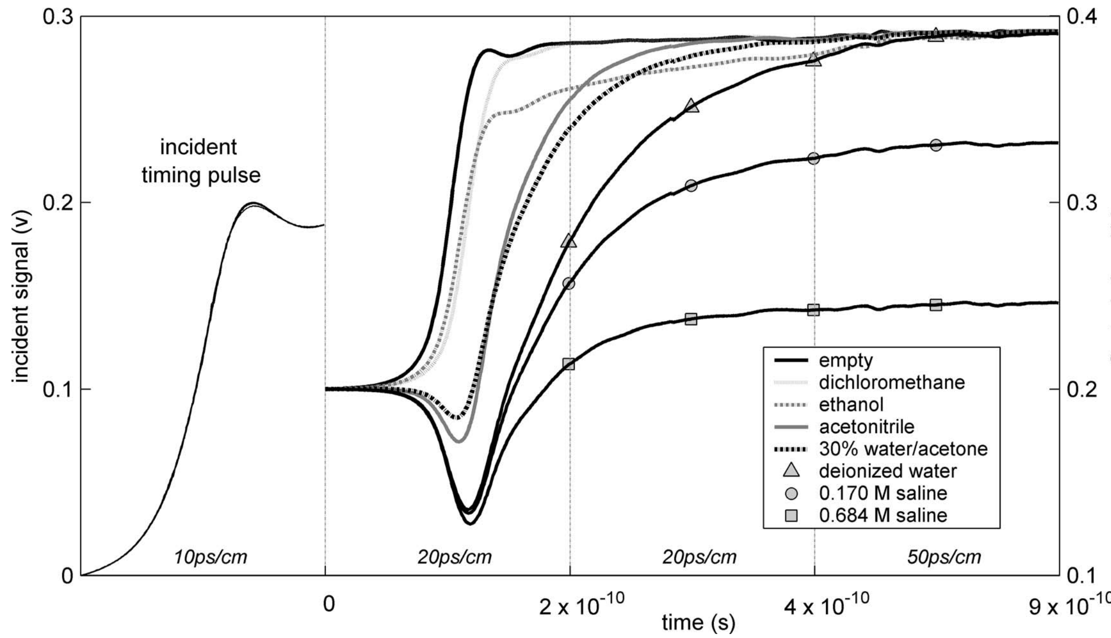

FIG. 1. Segmented transient acquisition for test liquids with 3.5-mm flat termination (four of 12 segments shown).

and immersed in the test liquid. This provides a terminating capacitance of around 25 fF into the sample material, as determined by calculating the reflection function ρ, matching to a known permittivity in the low-frequency limit, and working backwards to obtain the sensor capacitance C_o.

Reflected transients are shown in Figure 1 for various liquids including dichloromethane, acetonitrile, ethanol, and deionized water, as well as solutions of acetone, ethanol, and 0.170 M and 0.684 M saline. In each case segment 1 is the timing reference, segment 2 is the initial reflected transient, and segments 3–12 are the continuation of the initial reflected transient on increasing time scales. The empty sensor returns a positive reflection indicating the open-circuit reference, while the liquids return an increasing negative reflection whose exponential decay is governed by the loaded sensor capacitance and the 50 Ω (0.02 S) line impedance. The negative peak reflection amplitude decreases with increasing permittivity, and the exponential decay and superexponential stretching follows the changing permittivity and loss with frequency. In conducting salt solutions the superexponential stretching spans many decades due to ionic conduction and electrode polarization.

The corresponding Smith charts for the reflected transients are shown in Figure 2. The figure uses an admittance Smith chart, with susceptance/conductance circles originating from the left, displaying the terminating dielectric in the usual manner as a parallel combination of capacitance and conductance. Circles of constant susceptance and constant conductance are labeled, normalized to the 0.02 S (50 Ω) line admittance. For each transient, the Smith chart shows the load susceptance $\varepsilon' \omega C_o$ increasing with frequency, crossing lines of constant susceptance and tracing an arc around the lower

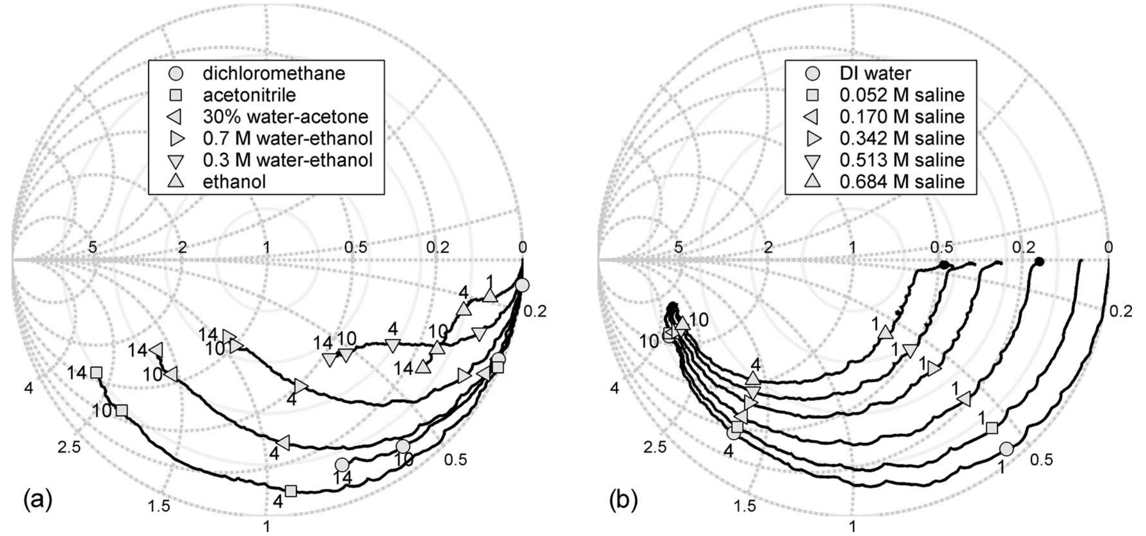

FIG. 2. TDR Smith charts for (a) increasing sample permittivity/loss (b) increasing sample conductivity. Frequency markers are shown in GHz.

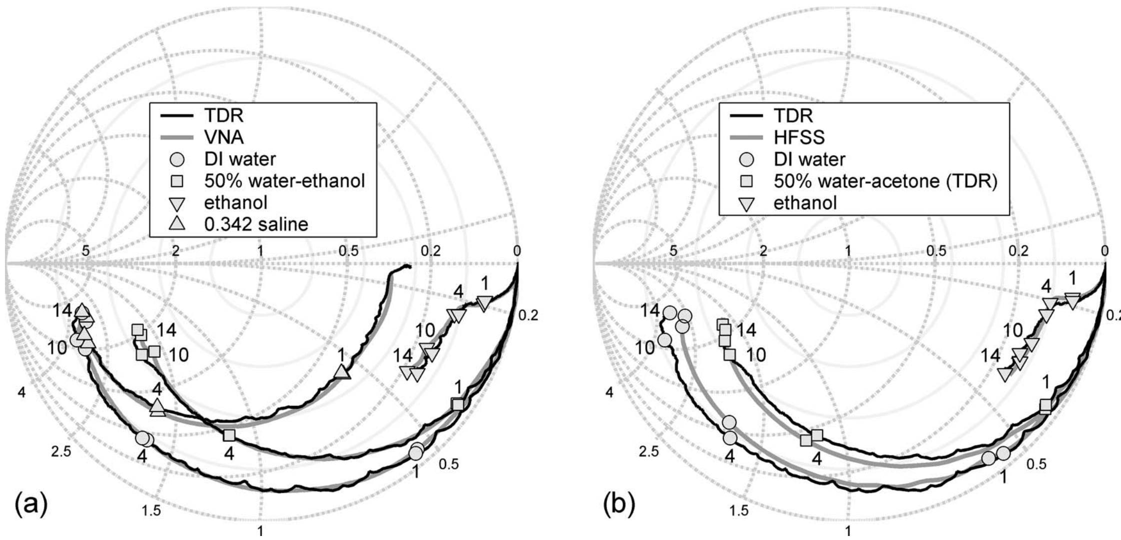

FIG. 3. TDR Smith charts compared with (a) VNA measurement and (b) HFSS simulation. Frequency markers are shown in GHz.

perimeter of the chart. Select frequency points are labeled on the diagram, starting at 1 GHz on the right and continuing to 14 GHz on the left.

Figure 2 illustrates the Smith chart behavior for typical variations in material properties. For an increasing real permittivity the measured susceptance $\varepsilon' \omega C_o$ increases more rapidly with frequency, showing a higher value at a given frequency and tracing a longer path around the lower perimeter of the diagram. This is clearly seen in Figure 2(a) for two low-loss liquids, comparing high-permittivity acetonitrile ($\varepsilon' = 37.5$) with low-permittivity dichloromethane ($\varepsilon' = 8.8$). For an increasing loss, the conductance $\varepsilon'' \omega C_o$ also increases with frequency, tracing a path which spirals inward on the diagram crossing both circles of constant conductance and constant susceptance. This is also seen in Figure 2(a), comparing liquids with increasing relaxation times τ such as acetonitrile (τ = 2-3 ps), 30% water/acetone solution (τ = 10.1 ps) (Ref. 7) and 0.7 M and 0.4 M water/ethanol solution (τ = 45–85 ps),[8] and pure ethanol (τ = 152 ps).[8] For the ethanol, a peak representing the loss characteristics and sensor capacitance is seen directly in the diagram around the relaxation frequency of $1/2\pi\tau$. For an increasing ionic conductivity, where the conductance remains constant over a wide frequency range,[2] the trace follows a constant conductance circle for each conductivity through the interior of the diagram. This is seen in Figure 2(b) for a series of water/salt solutions with increasing salt concentration and ionic conductivity. In addition, the very low frequency decrease in conductivity with electrode polarization is seen in the slight "hook" appearing below 100 MHz.

The TDR Smith chart can be compared with VNA measurements over the same frequency range. A 3.5-mm flat sensor with a 22-fF terminating capacitance is measured by TDR for several representative liquids. The sensor is then removed and connected to the VNA and measured again for the same liquids. The VNA is swept over the range of 50 MHz–20.05 GHz for both the empty sensor and measurement liquids, with the results time-gated and divided by the empty-sensor response to form the relative reflection coefficient Γ_{rel}, as explained previously. Results of both measurements are overlaid in Figure 3(a) for water, saline, and ethanol, and it is clear that the TDR and VNA data follow the same general behavior with the frequency markers at nearly identical positions. The VNA data is smoother as it has had a standard VNA calibration followed by a strict time gating applied, while the TDR data shows small fluctuations as internal calibration is precluded at this point by the constant switching of time scales.

The TDR Smith chart can also be compared with field simulation over the same frequency range. The same TDR data is shown in Figure 3(b), now overlaid with results of electromagnetic field simulation using HFSS for a 3.5-mm flat (zero pin length) termination. The TDR data and simulation results are similar, though there are small differences between the traces and the difference between corresponding frequency markers is larger. This results from a smaller simulation capacitance of 18.5 fF, because the simulation incorporates an ideal zero-length pin, while the grinding process leads to small metal burrs and other imperfections which make the capacitance larger than ideal. This difference does not significantly affect the reflection function ρ, which is normalized to the sensor capacitance (Eq. (2)), but does affect the reflection coefficient Γ_{rel} which is not. The difference is verified to be reduced by simulating the termination with a slight protruding pin, or by converting the simulated reflection coefficient Γ_{rel} to the reflection function ρ using the simulated sensor capacitance, and then converting back to the simulated reflection coefficient Γ_{rel} using the measured sensor capacitance.

The TDR Smith-chart display thus identifies basic features of the multi-GHz dielectric behavior for large variations in permittivity, loss, and conductivity. Smaller features involve artifacts due to the connector and sensor characteristics and require the full bilinear calibration. An advantage is that basic features are identified early, without the time-consuming multiple steps of calibration, such that any deviations from expected behavior can be corrected. Such deviations can include errors in Laplace transform, such as

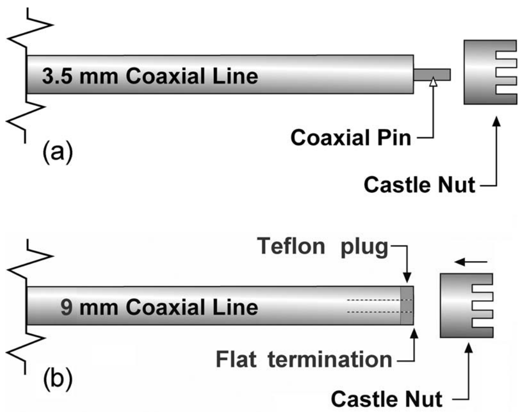

FIG. 4. TDR sensors for (a) 3.5-mm pin termination and (b) 9-mm flat termination.

improper integration cursors and baseline settings, improper truncation and tail fit settings, and excessive computation and noise. They can also include errors in acquisition, such as timing drift, segment mismatchs, connector artifacts, mechanical sensor damage, and sensor design to be discussed next.

B. 3.5-mm sensor: Pin termination

Many situations require a higher sensor capacitance to extend measurements to lower frequencies and lower permittivity materials while maintaining measurable susceptance. This is the case for cement hydration monitoring,[2] where bound water appearing around 100 MHz and grain polarization appearing around 1 MHz are also of interest. It is also true for a variety of biological and other organic/inorganic systems where both free and bound water and other molecular effects are of interest. Increasing the sensor capacitance is accomplished by extending the coaxial center conductor a short distance beyond the outer conductor as a protruding pin (Figure 4(a)) though this introduces artifacts which degrade high-frequency performance. Smith chart analysis helps in identifying these artifacts and quantifying the experimental trade-offs, which must be made to engineer for optimum performance.

Figure 5(a) shows the Smith chart for a 3.5-mm line with a 1.0-mm protruding pin in deionized water. The sensor is made by removing the outer conductor and teflon sleeve uniformly on a jeweler's lathe, trimming the pin to the desired length accurately on a Computer Numerical Control (CNC) machine, and removing any burrs near the pin under a microscope. The sensor capacitance is now 65 fF, as calculated from the low-frequency reflection function ρ, which represents a three-fold increase over the capacitance in Figure 3. The increase is seen in the Smith chart, where the 1 GHz frequency marker has now shifted clockwise around the lower perimeter of the diagram toward higher susceptance values. The capacitance can be verified from the diagram using the observed susceptance of 0.03 S at 1 GHz, a permittivity of 78 for water, and the expression $B = \omega\varepsilon C_o$.

An artifact of the longer pin is the large resonant loop appearing around 0.74 GHz. Here the sensor is in a beaker of water with a 54 mm inside diameter, filled 47 mm high, with the sensor vertical and approximately centered 20 mm from the bottom (position 1). If the sensor is measured twice the loop remains unchanged; however, if the sensor is moved laterally a few millimeters from the center (position 2) and measured again the loop changes shape while the rest of the diagram remains unchanged. This suggests reflections from sample boundaries as the cause,[9–11] with radiation emitted by the sensor reflecting back due to the high permittivity change between the water and surrounding container/air. Sample boundary reflections are confirmed by examining small differences between corresponding transients in the time domain. Successive transients are subtracted from one another and the difference enlarged, such that when the sensor is held fixed the difference is noise and when the sensor is moved a large delayed artifact appears starting around 1 ns. This is seen in Figure 5(b), where the 1-ns delay time is consistent with wave propagation with velocity $v = c/\sqrt{\varepsilon}$ within the beaker's sidewalls.

Sample boundary reflections are eliminated by surrounding the sensor pin with a serrated shield, which blocks

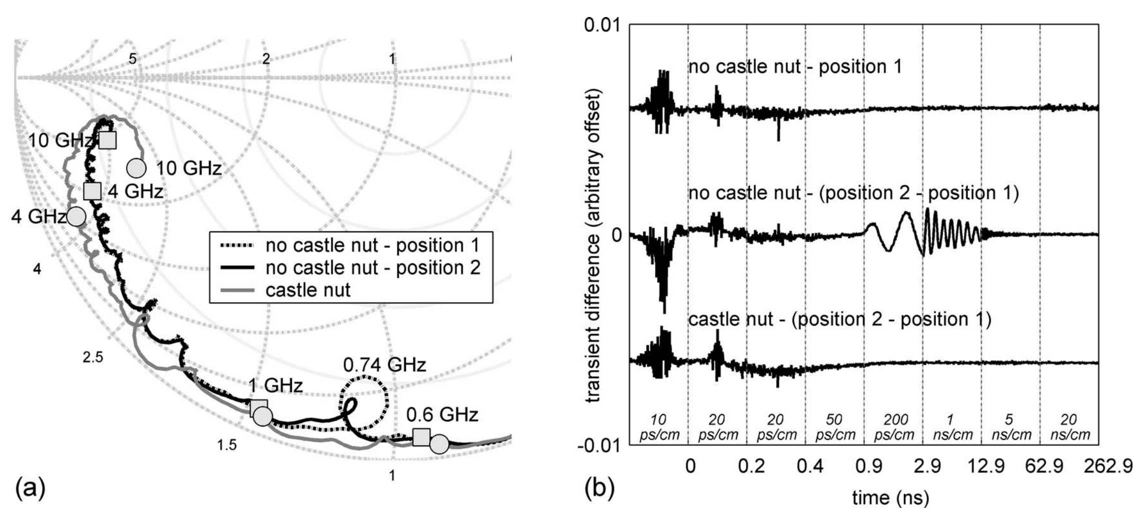

FIG. 5. Effect of sample boundary reflections and castle-nut shield on (a) Smith chart showing ~1 GHz resonance, (b) direct transient showing ~1 ns signal difference with sensor repositioning and its removal after introduction of the castle nut shield.

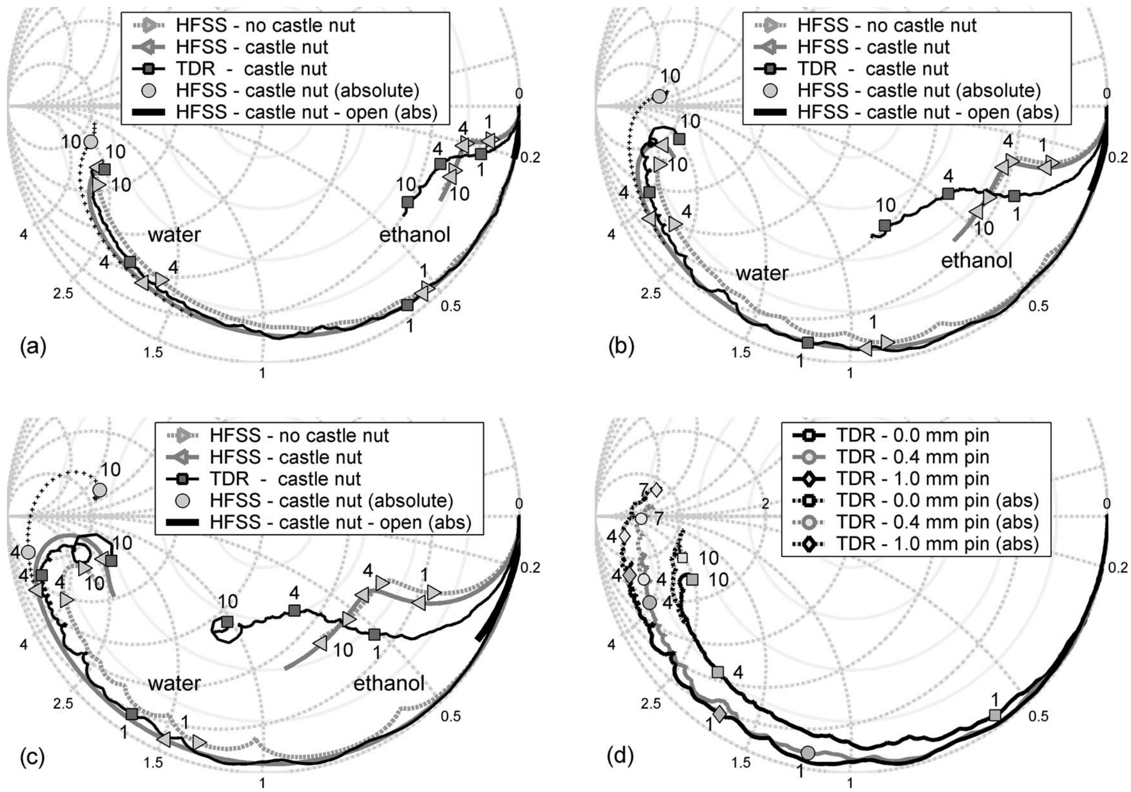

FIG. 6. Effect of varying pin length for 3.5-mm sensor and comparison with HFSS simulation for (a) 0.0-mm pin, (b) 0.4-mm pin, (c) and 1.0-mm pin. (d) Variation in TDR traces for water and correction to absolute reflection coefficient.

radiation leaving in a lateral direction while allowing free flow of the sample material past the pin. A 4.0 × 0.7-mm castle nut[12] works well for this purpose; the nut is reamed with a 3.58-mm (0.141″) drill and twisted onto the coaxial line with the base of the serrations aligned with the outer coax end. While the castle nut prevents lateral radiation and is easy to mount at the probe's end, as opposed to a smooth sleeve with continuous wall it also prevents the formation of air pockets trapped inside the nut when the probe is being immersed in a medium. As seen in Figure 5(a) the resonance loop is eliminated in the Smith chart, and in Figure 5(b) the transient difference after repositioning is eliminated as well. A small increase in capacitance is seen with the added ground plane, as the susceptance at labeled frequencies increases slightly.

C. 3.5-mm sensor: Variation in pin length

Figures 6(a)–6(c) show a series of TDR measurements using the coaxial pin configuration, where the pin is successively trimmed from 1.0 mm to 0.4 mm and to 0.0 mm on a CNC machine. In each case the pin is enclosed by a castle-nut shield, and the measured capacitances are 83 fF, 54 fF, and 23 fF, respectively. Starting with the 0.0-mm sensor in deionized water, the figure shows the effect of an increasing pin length is to shift the data clockwise around the lower perimeter of the Smith chart toward higher susceptance values, with the 1 and 4 GHz frequency markers moving accordingly. In addition, data on the left side of the diagram forms a "hook" with increasing pin length, in the frequency range around 10 GHz. For ethanol, the peak representing the loss characteristics also moves clockwise around in the diagram and enlarges, though no hook is seen in this case.

Superimposed on the TDR data is field simulations for the three pin lengths for both water and ethanol. Simulations are done both with and without the castle nut, though no sample boundary reflections should occur as the sample is treated as infinite. Nevertheless, without the castle nut irregularities do appear in deionized water at lower frequencies with increasing pin length, because of a slight reflection from the absorbing boundary in the finite element modeling which appears as a radiative effect occurring around 1 GHz. This artifact may be reduced by setting the absorbing boundary further away (a few wavelengths) from the sensor, but this demands more extensive simulation time and computational resources.

With the castle nut the artifacts due to sample boundary reflection are eliminated, and the data moves outward toward the perimeter of the Smith chart with the susceptance increasing slightly. The change is minimal for the 0.0-mm sensor but becomes more pronounced for the 1.0-mm sensor, with the result closely matching the TDR data. Overall, the deionized water simulation shows the same general features with increasing pin length as the TDR data, with the clockwise shift toward higher susceptance values, the "hook" appearing on the left, and the frequency markers generally aligning. The ethanol simulation shows the same loss peak behavior though the peak position is shifted due to the difference in measured and simulation capacitance described earlier. Changes for both water and ethanol are most rapid during the first 0.1–0.2 mm increase in pin length and more gradual thereafter.

The "hook" appearing on the left in water is an artifact of the relative reflection coefficient Γ_{rel} analysis, since the reflection coefficient is calculated relative to the empty-sensor reflection rather than the actual input stimulus. The input stimulus is not used in the TDR measurement since its timing is arbitrary relative to the sensor reflection, and since acquisition of the input stimulus over the relevant time scales would necessarily include the reflected pulse. The hook is removed by multiplying by the absolute reflection coefficient of the empty sensor, since the absolute reflection coefficient can be written as $\Gamma_x = \Gamma_{rel}\,\Gamma_r$ from Eq. (7). The absolute reflection coefficient of the empty sensor can be obtained either by simulation or by solving Eq. (1) for Γ_r with $\varepsilon = 1$,

$$\Gamma_r = \frac{v_{r,r}}{v_i} = \frac{G_c - i\omega C_o}{G_c + i\omega C_o}. \tag{8}$$

Figures 6(a)–6(c) also show the absolute reflection coefficient for each pin length in water obtained by simulation. For the 0.0-mm pin the deviation between relative and absolute reflection coefficients is small, while for the 0.4- and 1.0-mm pins it is much larger. The deviation becomes more pronounced at higher frequencies starting around 4 GHz and above (depending on pin length), which coincides with the frequency range of the absolute reflection coefficient crossing into the inductive region, showing resonance behavior with the sensor acting as an antenna. For the TDR data, the absolute reflection coefficient is estimated by multiplying the relative reflection coefficient by the simulated reflection coefficient of the empty sensor or by Eq. (8), where the simulation is slightly more accurate as it incorporates radiation effects of the empty sensor at high frequencies.

The absolute reflection coefficients for the three pin lengths are shown in Figure 6(d), and it is clear for the 0.4-mm and 1.0-mm pins that the data crosses into the inductive region in water in the 4–10 GHz range. For the 1.0-mm pin in water, the exact resonance frequency of the absolute reflection coefficient (where its angle becomes -180°) obtained by HFSS is 5.2 GHz with the castle nut (Figure 6(c), where the absolute reflection coefficient crosses the horizontal axis) and 7.2 GHz without it (not shown), which compares well with the quarter wave resonance of an ideal 1.0-mm long monopole antenna in water medium at about 8 GHz. For TDR Smith-chart display of the relative reflection coefficient, such a resonance is manifested by the presence of the mentioned hook in the corresponding trace. In addition, if Eq. (1) is rewritten in terms of the absolute reflection coefficient, similar to Eq. (6), the resulting real and imaginary components show rapid variation around the resonance frequency (where angle of $\Gamma_{abs} = -180^\circ$) as expected for quarter-wave behavior.[1]

D. 3.5-mm sensor: Effect on bilinear calibration

Artifacts revealed by Smith chart analysis can be traced through the bilinear calibration process to the final permittivity. For example, sample boundary reflections appearing in Figure 5 and pin artifacts appearing in Figure 6 enter into the reflection function $\rho(\omega)$ through Eq. (6). Two liquid measurements are required for each calibration, so artifacts appearing in $\rho_{\mathrm{cal},1}(\omega)$ and $\rho_{\mathrm{cal},2}(\omega)$ appear in the solution of simultaneous equations for $A(\omega)$ and $B(\omega)$ in Eq. (5). Artifacts appearing in $A(\omega)$ and $B(\omega)$ enter the unknown calibration through Eq. (4), and are compounded by similar artifacts appearing in the reflection function of the unknown $\rho_{\mathrm{unk}}(\omega)$ in the final result.

The propagation of these artifacts can be monitored by examining critical bilinear parameters for each pin configuration. A calibration is generated using 20% and 50% solutions of water in acetone as calibration references, which is then applied to an "unknown" solution of 40% water in acetone spaced between. Separate calibrations are generated for a 0.0-mm flat termination with castle-nut shield, a 1.0-mm pin configuration with castle-nut shield, and a 1.0-mm pin configuration without castle-nut shield. Figure 7(a) shows the bilinear $B'(\omega)$ parameter for each calibration, showing a small oscillation around 10 GHz for the 0.0 mm shielded pin, a much larger oscillation around 10 GHz for the 1.0-mm shielded and unshielded pins, and an additional artifact around 1 GHz for the 1.0-mm unshielded pin. Each of these artifacts is predicted by the corresponding Smith chart, with the 1 GHz artifact resulting from sample boundary reflections in Figure 5, and the 10 GHz artifact resulting from the sensor approaching the inductive region (i.e., resonance) in Figure 6. Similar behavior is seen in the term $1/|1\text{-}B\rho|$ in Figure 7(b), which monitors the development of computational poles in Eq. (4).

The effect of these artifacts on the calibrated permittivity is seen in Figures 7(c) and 7(d). For the 0.0-mm shielded pin, the real permittivity and the loss show a smooth variation to around 12 GHz with noise developing below 100 MHz. For the 1.0-mm pin with castle-nut shield the sensitivity below 100 MHz is improved though the permittivity and loss are severely distorted around 10 GHz. For the 1.0-mm pin without castle-nut shield the permittivity and loss are again distorted around 10 GHz, with an additional distortion appearing due to sample boundary reflections around 1 GHz. These distortions match corresponding distortions in bilinear parameters in Figures 7(a) and 7(b), and in each case the Smith chart foreshadows difficulties developing in the calibration process without performing the actual calibration.

E. 9-mm sensor: Variation in terminating plug thickness

Large diameter sensors intended for concrete hydration monitoring are made from a 9-mm diameter semirigid coaxial line obtained from Storm Products Company[13] of Woodridge, Illinois. The line is available in 1.5-m lengths (#421-227-3) with a standard N connector on one end, and the other end cut flat. The attenuation is 0.43 dB/m at 10 GHz, with the cutoff for the higher order coaxial mode at 14 GHz. The dielectric sleeve is low-density teflon, so the open end must be sealed with a solid teflon plug to prevent liquid ingress.

The 9-mm sensor is made by removing a short section of the low density teflon with a milling tool, which simultaneously reams both inner and outer conductor surfaces smooth. A slightly oversized teflon plug is pressed in mechanically, while applying a teflon etchant/epoxy around the edges if necessary to insure a tight seal. The surface is trimmed flat on a milling machine, adjusting the plug thickness to the

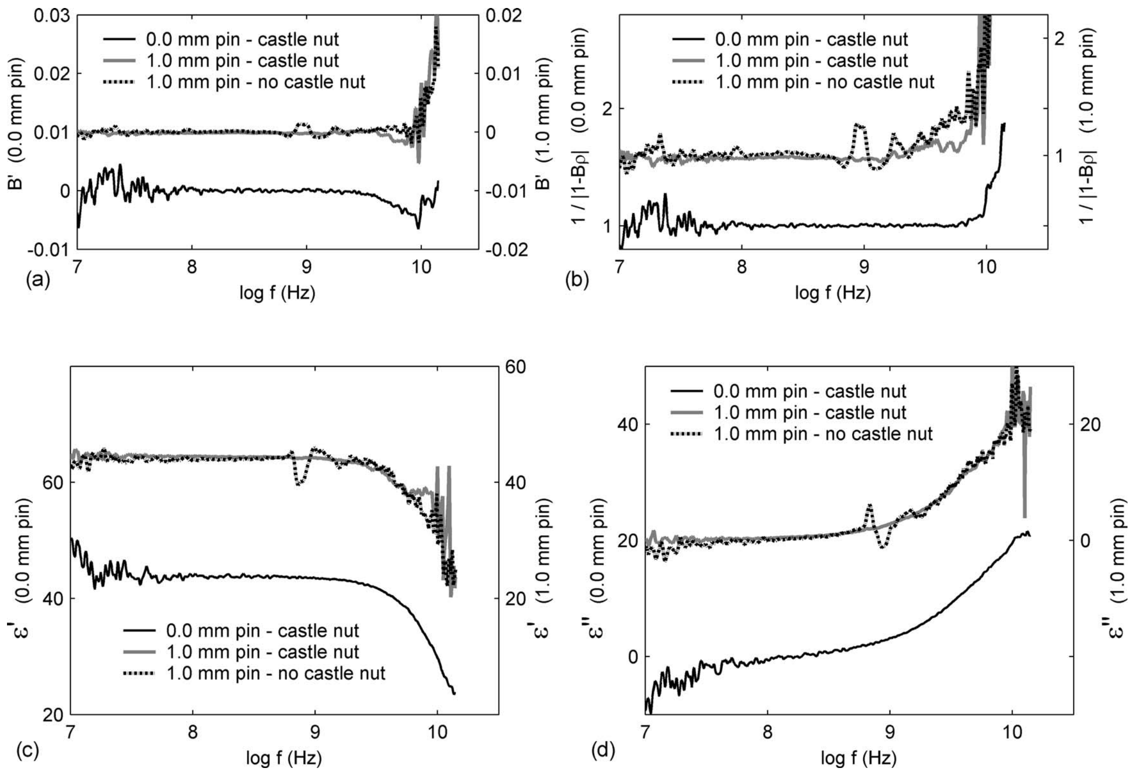

FIG. 7. Effect of pin length and castle-nut shield on bilinear parameters (a) B′, (b) 1 / |1-Bρ|, and calibrated permittivity (c) ε' and d) ε'' (3.5-mm sensor in 40% water/acetone solution).

desired length. The line is connected to the TDR input with an N-to-SMA adapter, mechanically clamping in place to insure no strain on the TDR input. To insure a consistent measurement plane, the sensor is leak-tested in acetone by monitoring the signal to make sure it remains constant over a period of time and returns to its original position when solvent is removed. The resulting sensor provides ∼60-fF load capacitance as shown in Figure 4(b).

Smith chart analysis shows that the sensor characteristics vary with the teflon plug thickness. Two 9-mm sensors are fabricated with plug thicknesses of 6.3 and 2.5 mm and immersed in deionized water. The reflected transients are captured and the resulting Smith charts shown in Figure 8(a) (without castle nut). For the 6.3-mm plug the trace follows a gradual path of increasing susceptance and conductance toward higher frequencies, while for the 2.5-mm plug the trace shows the frequency markers shifted to higher susceptance values and a sharp hook appearing around 4 GHz. The results are matched to VNA measurements for the same sensors in Figures 8(c) and 8(d), showing the same difference as well as alignment of the corresponding frequency markers. The cause of this difference is likely traced to the characteristic admittance discontinuity between the plug and the main 9-mm line, and the fact that the 6.3-mm plug thickness is a non-negligible fraction of the wavelength in the teflon plug, estimated to be around 50 mm at 4 GHz for $\varepsilon = 2$. This discontinuity causes the sensor's load admittance presented to the 50 Ω (0.02 S) line to vary with plug thickness, as seen both in the Smith chart and the reflection function $\rho(\omega)$ used in bilinear analysis.

F. 9-mm sensor: Effect of castle-nut shield

The 9-mm sensor is more susceptible to reflections from sample boundaries than the 3.5-mm sensor because of the larger diameter of the open end. The solution is to again surround the sensor with a castle-nut shield, though the larger shield diameter now allows waveguide modes propagating within the shield at relatively low frequencies. For example, a TM_{01} mode propagating in a cylindrical waveguide or radius 4.5 mm and real permittivity 76 (water around 3 GHz) has a cutoff frequency:[14]

$$f = \frac{2.405c}{2\pi r\sqrt{\varepsilon'}} = 2.92\ \text{GHz}. \tag{9}$$

In addition, the surface currents required for TM_{01} mode propagation are allowed by the castle nut's axial serrations while the surface currents required for TE_{11} mode (with a lower cutoff frequency) are not.

Figure 8(b) shows the 9-mm line with a 6.3-mm plug both with and without a 9-mm (3/8-in.-24) castle nut. The castle nut is reamed slightly and threaded onto the 9-mm line, with the base of the serrations aligned with the probe tip. As seen in the figure the castle nut introduces a sharp artifact at around 3.8 GHz, compared to the same sensor with no castle nut. A similar artifact is seen in the VNA comparison in Figure 8(e), and likely results from the TM_{01}-like mode propagating in the castle-nut shield. The artifact appears in the Smith chart Γ_{rel} display as well as the reflection function $\rho(\omega)$ used in bilinear analysis.

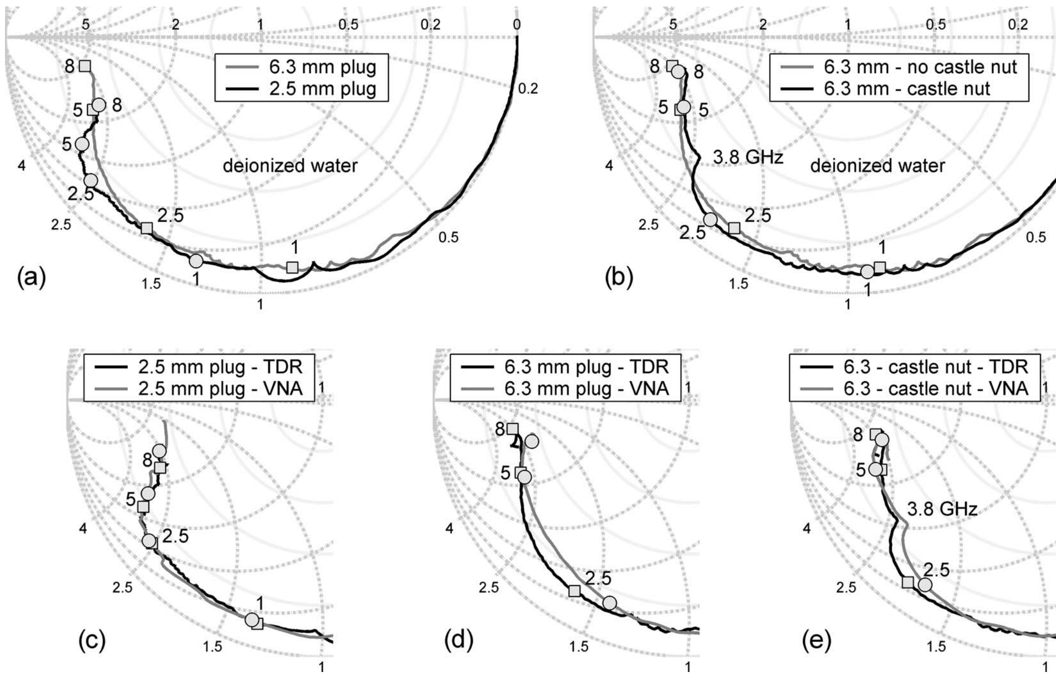

FIG. 8. Effect of terminating plug thickness and castle-nut shield on 9-mm flat termination in water. (a) 6.3 vs. 2.5-mm plug without castle-nut shield, (b) 6.3-mm plug with/without castle-nut shield, (c) 2.5-mm plug without castle-nut shield compared with VNA, (d) 6.3-mm plug without castle-nut shield compared with VNA, and (e) 6.3-mm plug with castle-nut shield compared with VNA.

V. DISCUSSION

We have demonstrated a TDR Smith-chart display to be a valuable diagnostic tool for a variety of situations in TDR dielectric spectroscopy. A relative reflection coefficient is formed by dividing the Laplace transform of the reflected sample transient by the Laplace transform of the empty-sensor transient and displaying it in the complex plane, with the approximate sensor admittance read from the susceptance and conductance circles. The Smith-chart display provides an initial estimate of the dielectric behavior in the multi-GHz range, as well as a means of identifying artifacts in acquisition or Laplace transform, in a way which does not require multiple steps of calibration and is only one step removed from the direct transient. Since the relative reflection coefficient is derived from the bilinear reflection function $\rho(\omega)$, artifacts occurring in the relative reflection coefficient foreshadow artifacts occurring in the bilinear calibration.

Results were presented for a simple 3.5-mm flat termination, showing variations in Smith chart behavior for typical variations in sample permittivity, loss, and, conductivity. Results were matched to VNA measurement over an identical frequency range, as well as to finite-element field simulation. Results were also presented for a 3.5-mm sensor with increased terminating pin lengths, typically employed at low frequencies and low permittivity media to increase sensor capacitance. Measurements were made as a function of pin length and compared with simulation, for pin lengths between 0.0 and 1.0 mm both with and without a surrounding shield. For an unshielded pin, the Smith chart analysis detects reflections from sample boundaries and provides a means of measuring the effectiveness of shielding used to eliminate these reflections. For a shielded pin, the Smith chart characterizes the effect of pin length on the susceptance variation and the admittance's approach toward resonance at high frequencies and high permittivity samples. A "hook" appearing at high frequencies at longer pin lengths was shown to be an artifact of the relative reflection coefficient, and a method for correcting it to an absolute reflection coefficient was explored. The effect of artifacts appearing in the Smith chart on the actual calibration was shown by tracking them through the calibration process to the final result. Finally, results were presented for a 9-mm flat termination used for concrete hydration monitoring, showing effects of the sensor's terminating admittance transformation within a terminating plug and the onset of waveguide modes in a surrounding shield, with results compared to VNA measurement.

It is well known that the admittance of an open-end sensor can deviate significantly from the simple air-terminated capacitance C_0 at multi-GHz frequencies.[3,15] The sensor can act as a resonating antenna, with the terminating admittance moving from capacitive to inductive region as seen in Figure 6. This resonance can produce artifacts which appear in the calibrated sample permittivity in Figure 7, which is impacted both by the choice of pin length and surrounding shield. Our preliminary studies suggest that an increase in pin length and the presence of a castle-nut shield lead to the resonance frequency moving to lower frequencies, and future work will include a quantification of this resonance limit for both the 3.5- and 9-mm sensors. Incorporation of the radiation model[3,15] in characterizing the unknown permittivity will be also studied.

ACKNOWLEDGMENTS

This work was supported in part by the National Science Foundation (NSF) under Grant No. 0700699.

[1] R. H. Cole, J. G. Berberian, S. Mashimo, G. Chryssikos, A. Burns, and E. Tombari, J. Appl. Phys. **66**, 793 (1989).
[2] N. E. Hager III and R. C. Domszy, J. Appl. Phys. **96**, 5117 (2004).
[3] D. Misra, M. Chabbra, B. R. Epstein, M. Mirotznik, and K. R. Foster, IEEE Trans. Microwave Theory Tech. **38**(1), 8 (1990).
[4] N. E. Hager III, Rev. Sci. Instrum. **65**, 887 (1994).
[5] F. 1. Mopsik, Rev. Sci. Instrum. **55**, 79 (1985).
[6] M. R. Tofighi and A. S. Daryoush, IEEE Trans. Instrum. Meas. **58**(7), 2316, (2009).
[7] A. C. Kumbharkhane, S. N. Helambe, M. P. Lokhande, S. Doraiswamy, and S. H, Mehrotra, Pramana, J. Phys. **46**(2), 91 (1996).
[8] S. Mashimo, T. Umehara, and H. Redlin, J. Chem. Phys. **95**(9), 6257 (1991).
[9] S. Evans and A. bin Azeman, Phys. Med. Biol. **43**, 2817 (1998).
[10] T. P. Marsland and S. Evans, IEE Proceedings H **134**(4), 341 (1987).
[11] D. M. Hagl, D. Popovic, S. C. Hagness, J. H. Booske, and M. Okoniewski, IEEE Trans. Microwave Theory Tech. **51**(4), 1194 (2003).
[12] Metric & Multistandard Components Corp., Hawthorne, NY, Part #935.
[13] Storm Products Company, Woodridge, Illinois, see www.stormproducts.com.
[14] S. Y. Liao, *Microwave Devices and Circuits* (Prentice-Hall, Englewood Cliffs, NJ, 1980), p. 119.
[15] A. Nyshadham, C. L. Sibbald, and S. S. Stuchly, IEEE Trans. Microwave Theory Tech. **40**(2), 305 (1992).